A dual-band adaptor for infrared imaging

A. G. McLean,[1,a),b)] J-W. Ahn,[1] R. Maingi,[1] T. K. Gray,[1] and A. L. Roquemore[2]
[1]*Oak Ridge National Laboratory, Oak Ridge, Tennessee 37831, USA*
[2]*Princeton Plasma Physics Laboratory, Princeton, New Jersey 08543, USA*

(Received 22 March 2012; accepted 27 April 2012; published online 21 May 2012)

A novel imaging adaptor providing the capability to extend a standard single-band infrared (IR) camera into a two-color or dual-band device has been developed for application to high-speed IR thermography on the National Spherical Tokamak Experiment (NSTX). Temperature measurement with two-band infrared imaging has the advantage of being mostly independent of surface emissivity, which may vary significantly in the liquid lithium divertor installed on NSTX as compared to that of an all-carbon first wall. In order to take advantage of the high-speed capability of the existing IR camera at NSTX (1.6–6.2 kHz frame rate), a commercial visible-range optical splitter was extensively modified to operate in the medium wavelength and long wavelength IR. This two-band IR adapter utilizes a dichroic beamsplitter, which reflects 4–6 μm wavelengths and transmits 7–10 μm wavelength radiation, each with >95% efficiency and projects each IR channel image side-by-side on the camera's detector. Cutoff filters are used in each IR channel, and ZnSe imaging optics and mirrors optimized for broadband IR use are incorporated into the design. *In-situ* and *ex-situ* temperature calibration and preliminary data of the NSTX divertor during plasma discharges are presented, with contrasting results for dual-band vs. single-band IR operation. © *2012 American Institute of Physics*. [http://dx.doi.org/10.1063/1.4717672]

I. INTRODUCTION

In late 2009, National Spherical Tokamak Experiment (NSTX) (Ref. 1) replaced existing graphite tiles with a circumferential liquid lithium divertor (LLD) module[2] in the lower outboard divertor (0.66 cm < R < 0.85 cm) in order to improve density control, lower edge collisionality and impurity influx, and enhance power handling capability.[3] Liquid Li has a high capacity for hydrogenic retention and extraction/removal, and introduces the ability of self-healing for the plasma-facing surface to tokamak devices. While graphite has relatively low optical reflectivity at infrared (IR) wavelengths (R < 0.15),[4] liquid Li is highly reflective (R > 0.9).[5] Additionally, emissivity of Li varies significantly with temperature (as described by the Hagen-Rubens model[6,7]), and can vary significantly as fuel and impurities are absorbed into the plasma-facing surface. The latter effect leads to creation of molecules (LiH, Li_2C_2, Li_2CO_3) whose individual emissivities are difficult to measure *ex-situ* in a controlled manner,[8] or measure *in-situ* with high spatial and temporal resolution[9] then predict their value at wavelengths commonly measured by IR cameras.[10] Each of these challenges greatly complicates interpretation of infrared photon flux from plasma-facing surfaces in NSTX which, near the divertor, can be subject to temperatures of >1000 °C and heat fluxes of >10 MW/m^2 that typically exist for brief intervals (<5 ms in the reviewed present data).[11] This high heat flux makes the capability to diagnose surface conditions using IR with sufficient temporal and spatial resolution essential for successful operation of the LLD.

To overcome the interpretive complications which ensue due to extensive use of Li in the NSTX divertor, a dual-band adaptor for existing IR cameras has been developed. This device utilizes the ratio of measured radiant energy in two integrated IR wavelength regions, instead of the integrated intensity of a single IR band alone as in traditional IR cameras (e.g., 3–5 μm for indium antimonide (InSb) and mercury cadmium telluride (MCT), and 8–13 μm for vanadium oxide-based microbolometers.) While the single-band brightness technique is susceptible to signal attenuation (e.g., due to contaminated optics or accumulation of dust over time) or enhancement due to variable emissivity of the measured object (e.g., due to changes in temperature and varying surface composition), the dual-band approach is based on the ratio of the intensities of two separate signals which should be attenuated or enhanced equally, implying that the ratio stays constant for a given surface temperature despite attenuation or changes in target emissivity. Unfortunately, the dual-band approach does not improve infrared interpretation in the presence of significant reflections (i.e., in a tokamak with an all-metallic plasma-facing wall); this potential complication still depends on advanced optical modelling for adequate resolution, e.g., Refs. 12 and 13. Based on (a) the geometry of the LLD in NSTX and the lack of susceptibility to specular reflection by local surfaces, and (b) empirical observation of plasmas with different up-down symmetry in NSTX, however, the contribution of reflections to measured infrared intensities in the lower divertor is estimated at <10%.

Provided the optical technology exists with sufficient spectral discrimination, this same ratio technique can be extended to multiple IR bands (i.e., three or more) or colors (i.e.,

a)Author to whom correspondence should be addressed. Electronic mail: amclean@pppl.gov.
b)This research was performed while A. McLean was at Princeton Plasma Physics Laboratory (PPPL), Princeton, New Jersey 08543, USA.

separate spectral bandwidths within the same IR band) with associated improvements in measurement quality and accuracy. These IR bands/colors may include all or portions of the near IR (NIR, 0.7–1.0 μm), short wavelength IR (SWIR, 1.0–3.0 μm), medium wavelength IR (MWIR, 3.0–5.0 μm), long wavelength IR (LWIR, 7.0–12.0 μm), and very-long wavelength IR (VLWIR, 12.0–30.0 μm). For purposes of monitoring the plasma-heated divertor of a tokamak, however, interpretation of the integrated NIR and SWIR regions are avoided due to spectral contamination primarily from molecular emissions.[14,15]

At the time of writing, no similar optically based IR splitting imaging system as described has been developed or pursued that the authors can identify. While dual-color and dual-band IR pyrometers are common,[16] and camera systems that integrate two separate quantum well infrared photodetector or MCT) IR sensors in a single detector in a sandwich, or "superlattice" package are under development by a number of IR camera suppliers, including FLIR (USA), QmagiQ (USA), AIM Infrarot-Module (Germany), and IR-CAM/Thermosensorik (Germany), their current capabilities are limited compared to those of present generation single-band IR cameras. In readout speed, dual-band detectors are currently limited to a maximum throughput of <40 Mpixels/s, (i.e., a frame of ≤300 Hz at 384 × 288 pixels) compared to >140 Mpixel/s attained by existing MWIR and LWIR cameras from these and other manufacturers – this is significantly less than that adequate for study of transient phenomena in NSTX and other fusion devices (>1000 Hz required). In addition, these new dual-band systems are expensive, and require very long lead times (typically 3–6 months). At the expense of loss of 1/2 the measured resolution in one imaging dimension, the dual-band imaging adaptor for existing single-band IR cameras described here has no inherent speed limitation (i.e., the speed of a single-band camera pair with the dual-band adapter is limited only by the capabilities of the camera alone), and at a low incremental hardware cost.

II. THEORETICAL PREDICTION OF DUAL-BAND RATIO DEPENDENCE ON TEMPERATURE

Planck's Law allows quantification of the spectral photon emittance, Q (aka, exitance) of a perfect thermal radiation emitter – a black body (BB) source – according to the expression

$$Q_{\lambda,BB}(\lambda,T) = \frac{2\pi c}{\lambda^4 \times \left[\exp\left(\frac{hc}{\lambda kT}\right) - 1\right]} \times [\text{photons s}^{-1}\,\text{m}^{-2}\,\text{nm}^{-1}], \quad (1)$$

where c is the speed of light, λ is the photon wavelength, h is Planck's constant, k is the Boltzmann constant, and T is the temperature of the BB source. Photon emittance may then be converted to spectral radiant emittance, W (aka, spectral radiance) using

$$W(\lambda,T) = \frac{hc}{\lambda} Q(\lambda,T), \quad (2)$$

giving

$$I_{\lambda,BB}(\lambda,T) = \frac{2\pi hc^2}{\lambda^5 \times \left[\exp\left(\frac{hc}{\lambda kT}\right) - 1\right]} [\text{W m}^{-2}\,\text{nm}^{-1}]. \quad (3)$$

For mathematical simplicity, it is assumed that $\exp(hc/\lambda kT) \gg 1$, leading to the expression

$$I_{\lambda,BB}(\lambda,T) \cong \frac{2\pi hc^2}{\lambda^5 \times \left[\exp\left(\frac{hc}{\lambda kT}\right)\right]}. \quad (4)$$

For a real surface composed of material m, the spectral radiant emittance is equal to some fractional magnitude relative to a BB emitter. Like a BB source, this value is dependent on λ and T, and, in addition, it may have dependence on the direction of observation, θ and φ (zenith and azimuthal angle, respectively) depending on surface roughness, as

$$I_{\lambda,surf}(\lambda,T,\theta,\phi) = \varepsilon_{\lambda,m}(\lambda,T,\theta,\phi) \times I_{\lambda,BB}(\lambda,T), \quad (5)$$

where $\varepsilon_{\lambda,m}$ is the spectral emissivity for material m at a given temperature and observational direction. For interpretation of the spectral radiant emittance in two separate spectral bands with intensity-averaged wavelengths λ_1 and λ_2, the emittance ratio is expressed as

$$\frac{I_{\lambda_1,surf}}{I_{\lambda_2,surf}} = \frac{\varepsilon_{\lambda_1,m}}{\varepsilon_{\lambda_2,m}} \times \frac{I_{\lambda_1,BB}}{I_{\lambda_2,BB}}. \quad (6)$$

Substituting Eq. (4) into this expression and rearranging for T gives the following:

$$T = \frac{hc}{k} \times \frac{\left(\frac{1}{\lambda_2} - \frac{1}{\lambda_1}\right)}{\left[\ln\left(\frac{\varepsilon_{\lambda_2,m}}{\varepsilon_{\lambda_1,m}}\right) + \ln\left(\frac{I_{\lambda_1,surf}}{I_{\lambda_2,surf}}\right) + \ln\left(\frac{\lambda_1^5}{\lambda_2^5}\right)\right]} [\text{K}]. \quad (7)$$

This straightforward expression demonstrates that T is dependent on the observed wavelength bands λ_1 and λ_2, the ratio of spectral radiant emittance released in each wavelength band, $I_{\lambda_1,surf}/I_{\lambda_2,surf}$ (i.e., the relative intensity ratio), and the ratio of spectral emissivity for the material within each wavelength band, $\varepsilon_{\lambda_1,m}$ and $\varepsilon_{\lambda_2,m}$. If the observed material has $\varepsilon < 1.0$ but equal for all observed wavelengths, it is referred to as a "gray body." The assumption of a gray body is commonly appropriate for opaque materials with relatively high ε (i.e., low R, such as graphite). For materials with low ε (i.e., high R, like liquid lithium), variable emissivity may be introduced by variation in optical conductivity (i.e., for a flat metallic surface), and due to the physical size of microscopic features on the surface of the material including texture and oxide growth. Under plasma bombardment as experienced by the Li surface in NSTX, surface roughness is ~100 μm,[17] thus optical roughness, σ/λ, is >10 at all observed IR wavelengths (i.e., the "geometric" surface emissivity categorization[18]). The surface is therefore sufficiently thick to be optically diffuse at all wavelengths,

reducing the impact of wavelength on emissivity for the surface. Theoretical analysis of surface emissivity of liquid Li from 200–1700 °C has been carried out in Ref. 19 and found to vary minimally (<∼10%) in the range of 4–10 μm. This result is confirmed by observations of a similar metal, Gallium, in Ref. 20 where theoretical variability in emissivity was found to be similar to that of Li in the range of 2–5 μm, and that result confirmed experimentally through a temperature range of 150–400 °C. Note also that even this low level of non-gray body behavior is believed to be reduced by the presence of impurities in the plasma-facing surface which will increase the effective emissivity of the surface with respect to a pure metal layer.

III. DUAL-BAND OPTICAL ADAPTOR DESIGN

The dual-band imaging adaptor was designed for initial demonstration on the existing high-speed IR camera operated at NSTX by ORNL staff, a Santa Barbara Focal Plane (SBFP) ImagIR camera incorporating a 128 × 128, 40 μm pixel broadband mercury cadmium telluride (HgCdTe) LN_2 cooled detector (QE > 90% within 1.5–11 μm, 14-bit output, <20 mK typical noise equivalent temperature difference (NETD), <0.1 μs error in integration time turn on and turn off.)[21] In typical wideband operation, the camera utilizes either a 25 mm, *f*#2.3 Janos Technology Varia or Ninox lenses which each provide a 15.5° field of view (FOV), and transmit the 8–12 μm/3–12 μm waveband with T_{avg} ∼ 95%/∼75%, respectively. In dual-band operation, a 25 cm long imaging adapter which contains all necessary optics to separate incoming light into MWIR and LWIR bands is mounted between the IR camera and lens, and carefully aligned and focused for operation on the machine.

The key enabling technology for the dual-band imaging adapter is a long-wave pass dichroic beamsplitter which efficiently separates MWIR and LWIR photons. For this project, Lambda Research Optics[22] developed a dichroic which, when mounted at 45° to the impinging optical path, transmits the 7–10 μm (LWIR) spectral band (λ_1) with T_{avg} ∼ 92% efficiency, and reflects the 4–6 μm (MWIR) spectral band (λ_2) with R_{avg} ∼ 99% efficiency. At the longer wavelength the assumption made in Sec. II that exp ($hc/\lambda kT$) ≫ 1 begins to deteriorate for temperatures ≥∼500 °C (Figure 1), which is well below the plasma-facing surface temperature reached during fast transient events (e.g., "edge localized modes" or ELMs) in tokamaks. For this reason, evaluation of the expressions for the ratio of spectral radiant emittance in Sec. II is carried out numerically without the assumption for the exponential in Sec. IV.

The optical platform for the dual-band imaging adapter is a commercial image splitter, the OptoSplit II, manufactured by CAIRN Research.[23] Operating in the visible wavelengths by default, this device projects each wavelength region (i.e., each optical "channel"), side-by-side, each onto one-half of the same detector (Figure 2). The splitter provides the capability for precision multi-axis optical alignment, fine focusing, and the flexibility to incorporate optical elements different from those which it uses in its standard configuration.

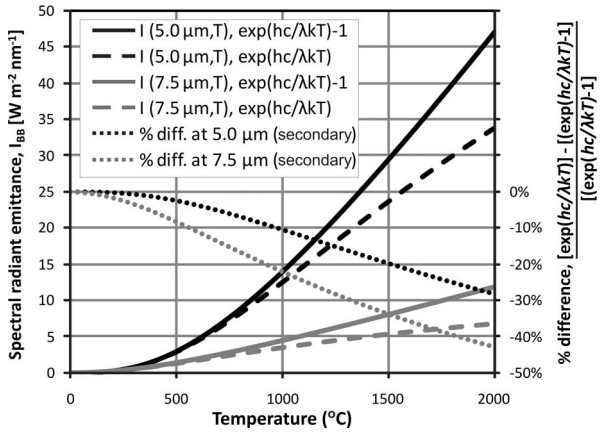

FIG. 1. The applicability of the exp ($hc/\lambda kT$) ≫ 1 approximation to evaluation of Planck's law. Spectral radiant emittance from a blackbody source, I_{BB}, is shown versus surface temperature. Percent difference between the calculated value using the exact and approximated expression is shown on the secondary axis.

Achromatic doublets optimized for the visible spectrum which were utilized in the input and output ends of the OptoSplit II were replaced initially with uncoated zinc selenide (ZnSe) meniscus lenses (T_{avg} ∼ 60%–70% for 0.8–15 μm) manufactured by II-VI Infrared.[24] The refractive index of ZnSe, however, varies significantly from 4 μm to 10 μm resulting in considerable chromatic aberration across the observed waveband (∼2 mm chromatic focal shift). After their initial demonstration, the meniscus lenses were replaced with diffractive optical element (DOE) hybrid singlet lenses,[25,26] also manufactured by II-VI Infrared, applied with a broadband AR coating (T_{avg} > 95% for 2.5–12 μm). Once incorporated, these elements significantly improved the signal-to-noise ratio (SNR), reduced astigmatism (∼1 mm compared to ∼2 mm), reduced spherical aberration (∼0.5 mm compared to ∼1 mm), and reduced chromatic aberration (<0.2 mm chromatic focal shift, or a 10× improvement). Diffraction efficiency and the significance of non-design order illumination[27] in the field of view at the observed spatial resolution was not found to detrimentally affect their imaging performance.

Shortwave pass and longwave pass cutoff filters produced by Raynard Corporation[28] are used on each wavelength

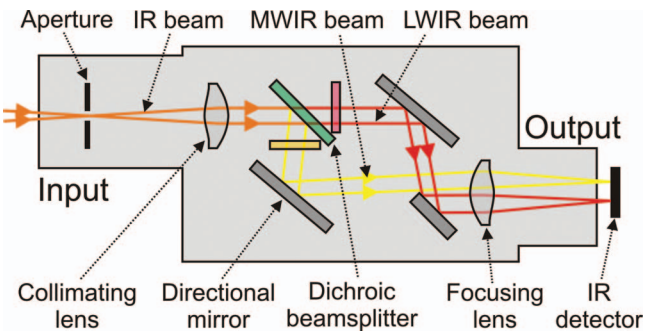

FIG. 2. Schematic of the dual-band infrared adapter. Incoming light is separated into two bands by a dichroic beamsplitter then re-directed to be imaged side-by-side on the detector of the infrared camera. Lenses at the input and output ends of the splitter collimate and focus the beam, respectively.

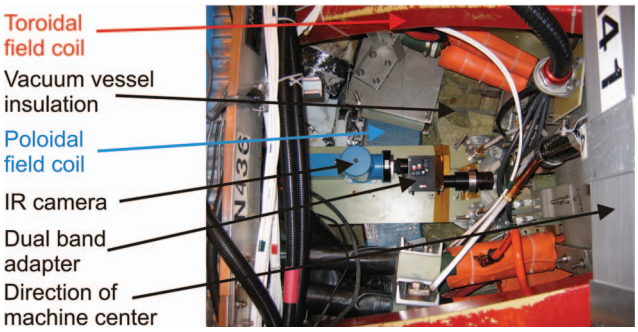

FIG. 3. Image showing the fast IR camera paired with the dual-band adapter attached to the top of the NSTX device.

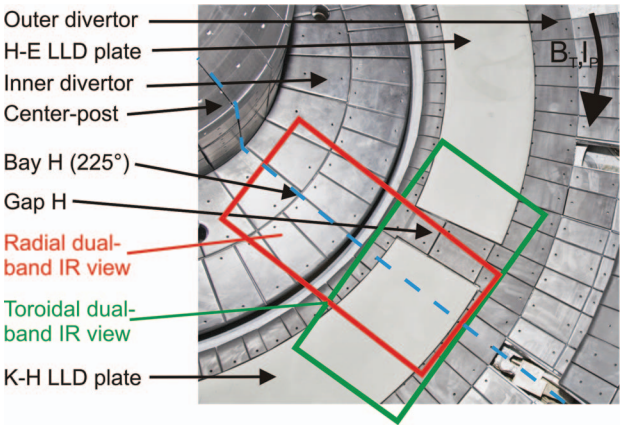

FIG. 4. Visible view of the NSTX lower divertor near Bay H (225° toroidally) showing graphite armor tiles, and the locations of the LLD plates. The extent of the FOV for the two-color IR camera is also shown in both radial and toroidal-view configurations.

band in order to limit the MWIR band to only thermal IR emission, remove band overlap, and prevent undesirable stray light from outside both channels. Cutoff filters were selected based on a compromise between (a) error reduction in the measurement acquired by increasing the separation between the sensitivity-weighted mean wavelengths between the location of the two observed bands, and (b) the desire to maximize utilization of the spectral region where the detector is sensitive. Dielectrically coated protected silver mirrors with $R_{avg} > 98\%$ throughout the 4–10 μm spectral band are used to redirect the two optical paths. Finally, custom adapters were designed for the appropriate difference in back focal length and manufactured to most directly connect the existing OptoSplit II input and output C-mounts to Bayonet mounts utilized by the SBFP camera and Janos IR lens. The assembled IR camera with dual-band imaging adapter attached is shown installed on the NSTX device at the 225° toroidal location ("Bay H") in Figure 3. The area observed by the camera at this position inside the NSTX device is shown in Figure 4 in each of two allowable orientations provided by rotating the dual-band imaging adaptor: In the first "radial" configuration, the most prominent surface features observed are the graphite tiles of the inner divertor, and the LLD plate at the outer divertor on which Li collects during evaporation procedures. In the second "toroidal" configuration, the dual-band IR camera is positioned to view the outer divertor only such that measurements may be made of two separate LLD plates as well as the graphite tiles which sit between them (i.e., in "Gap H").

Overall optical transmission for each component of the dual-band imaging adapter and for the full IR system is shown in Table I. Transmission figures are shown to compare single-color and dual-band operation. In standard single-band operation, typical integration time which maximizes available dynamic range (DR) of the detector is 5–10 μs per frame; at the maximum full-frame capture rate (1.6 kHz), this implies a duty cycle of 0.8%–1.6%. With the dual-band imaging adapter (using the meniscus lenses) connected, integration time to achieve similar signal is found to increase to 50–75 μs per frame (i.e., an 8%–12% duty cycle) with an associated increase in dark current and ~30% reduction of available DR. Overall transmission would be improved with a BB AR coating applied to the ZnSe vacuum window at the Bay H port (T_{avg} from ~70% to >95%) which is planned for the future.

TABLE I. Theoretical component-based average transmission for optical arrangements.

Optical element		Single-band operation		Dual-band operation meniscus lenses		Dual-band operation DOE lenses	
		8–12 μm operation	3–12 μm operation	4–6 μm band	7–10 μm band	4–6 μm band	7–10 μm band
Observed bandwidth		4 μm	9 μm	2 μm	3 μm	2 μm	3 μm
Bay H port window		98%	83%	70%	96%	70%	96%
Perp. View mirror		98%					
IR primary lens		95%	75%				
Dual-band adapter	Input lens	N/A		70%	72%	95%	97%
	Mirror 1	N/A		98%			
	Dichroic	N/A		99%	92%	99%	92%
	Short pass filter	N/A		N/A	83%	N/A	83%
	Long pass filter	N/A		95%	90%	95%	90%
	Mirror 2	N/A		98%			
	Output lens	N/A		70%	72%	95%	97%
Camera window		95%	96%	97%	97%	97%	97%
Dual-band adapter overall		N/A		44%	34%	82%	62%
Overall transmission		87%	59%	22%	23%	41%	43%

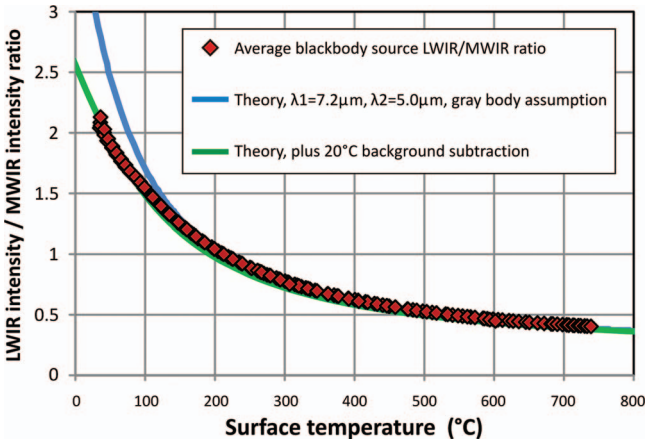

FIG. 5. Relationship between the integrated LWIR/MWIR intensity ratio and the surface temperature measured using a BB source for T_{surf} = 50–750 °C. The solution to theoretical relationship for the curve (Eq. (6)) is also shown. Typical error in measured temperature of the BB source (x axis) is ±1 °C, and that of the measured intensity ratio (y axis) is ±0.02.

IV. CALIBRATION METHODS

Demonstration of the dual-band IR adaptor was first accomplished *ex-situ* with the SBFP ImagIR camera via absolute temperature calibration using an Electro Optical Industries WS162 blackbody source capable of operation at up to 750 °C. Data were captured at five separate integration times, T_{int}, from 10 to 75 μs in order to determine the value at which use of the dynamic range of the camera (i.e., before saturation is reached in either wavelength band) is maximized. Data are analyzed by first subtracting a no-light exposure with the same integration time, then determining the average and the standard deviation of a maximal portion of each channel on the exposed detector. The resulting plot of the *ex-situ* data is shown in Figure 5. It is found that the non-saturating LWIR/MWIR ratio for all integration times in the bounds listed above follow the same trend-line overlap with high coincidence. This is a verification of the linearity of the detector response and a positive demonstration that calibration of the ratio versus surface temperature curve can be simplified to a single function independent of the integration time used by the camera. Saturation is found to occur at the two highest integration times, T_{int} = 50 and 75 μs, first in the MWIR channel in each case, followed by the LWIR channel for T_{int} = 75 μs.

For comparison to theory, numerical evaluation of the spectral radiant emittance ratio, $I_{\lambda_1,surf}/I_{\lambda_2,surf}$ (Eq. (3)) is also plotted with the following parameters applied: λ_1 = 7.2 μm, λ_2 = 5.0 μm, $\varepsilon_{\lambda_1,m}$, and $\varepsilon_{\lambda_2,m}$ = 0.99 (appropriate for the BB source used in this test). Additionally, evaluation of the theoretical curve with application of a background subtraction of a uniform 20 °C background – replicating the background subtraction procedure utilized on experimental data captured while observing the BB source – is carried out and plotted. Correlation between theory and the experimental data is excellent, giving a significant measure of confidence in application of the dual-band IR technique. It is seen that the region where the derivative of the ratio-to-temperature relationship is the greatest – in the range of ~50–500 °C – is the same region where the majority of surface temperature measurements will be found in the NSTX device. While the curve flattens significantly above this value (i.e., below a ratio of ~0.5), note that the signal measured in each wavelength region also approaches its un-saturated maximum intensity at the same time; thus the SNR is maximized.

For efficient application to data collected during NSTX operation, unsaturated data for the integrated measured emission intensity ratio, $I_{\lambda_1,surf}/I_{\lambda_2,surf}$, is related to the surface temperature of the BB source using a high order polynomial fit. Coefficients are least-squares fit to the available experimental data using the TableCurve 2-D software package. Additionally, individual integrated band intensities – $I_{\lambda_1,surf}$ for the integrated LWIR band and $I_{\lambda_2,surf}$ for the integrated MWIR band – are related to the temperature of the BB source using a polynomial at each integration time; this is carried out in order to allow for calibrated single-band interpretation of data collected by the camera with the dual-band adapter attached.

The calibration process is then repeated with the camera viewing the LLD plates in the NSTX divertor during their electrical heating, i.e., without plasma exposure. During integrated testing and demonstration of the LLD, the plates were heated in a controlled manner from room temperature to their maximum rated temperature of 250–320 °C over an ~1–2 h period, well beyond the melting point for pure lithium of 180 °C. On the NSTX machine (Figure 3), the camera views downwards into the vacuum vessel from the upper Bay H port via an ~45 ° angled mirror through a ZnSe window anti-reflected (AR) coated to enhance transmission in the 8–12 μm spectral band (see Table I). Due to restricted machine access when the LLD is in operation, the primary lens of the fast IR camera is pre-focused observing a heat source in a laboratory at a distance of 3.4 m, equal to the distance between the camera's lens and the NSTX divertor floor. Analysis of data captured during LLD heating is shown in Figure 5. Temporal response from five thermocouples embedded in the copper substrate of the K-H quadrant LLD plate and within the observed area of the fast IR camera are analyzed and compared to the measured integrated band intensity ratio on the IR detector. The resulting $I_{\lambda_1,surf}/I_{\lambda_2,surf}$ (i.e., LWIR/MWIR) intensity ratio for *in-situ* measurement is shown overlapped with the *ex-situ* data taken with the BB source in Figure 6. The integrated, background-subtracted signal in the MWIR band is measured to be attenuated by 41% compared to the *ex-situ* calibration viewing the blackbody source; this is primarily due to the lack of an AR-coating which would enhance transmission of the 4–6 μm spectral region on the Bay H ZnSe window. The accumulation of dust and dirt present in the NSTX test cell (NTC) on the top face of the window, and potential deposits of Li and C-containing compounds on the vacuum face are also thought to be a significant contributor. Integrated signal in the LWIR band is also found to be attenuated compared to the *ex-situ* result, but the signal loss is found to be less at 34%, likely primarily due to accumulation of dust, dirt, and deposits, but also erosion of the AR-coating on the window during ultrasonic cleaning procedures carried out over its lifetime. The result of losses in both spectral regions is a 14% increase in the LWIR/MWIR ratio as measured

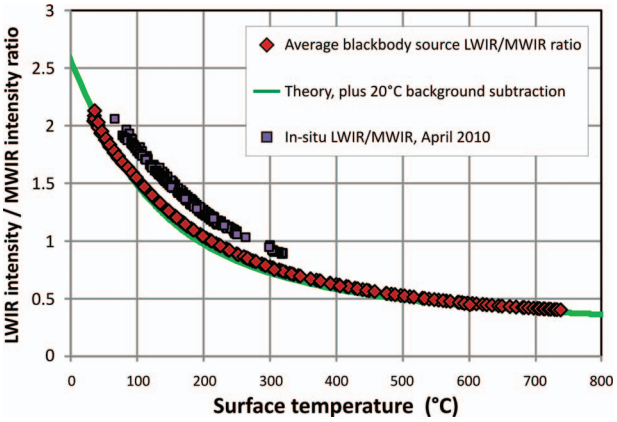

FIG. 6. Integrated LWIR/MWIR intensity ratio measured experimentally both *ex-situ* with a BB source, and *in-situ* by monitoring of the LLD surface during heating to 320 °C. Data collected in both situations are found to be well fit to functions of the same form.

in-situ compared to the *ex-situ* result. Due to significant available margin in terms of integration time (and thus dark current and ultimately signal-to-noise ratio and dynamic range), the reduction in optical transmission is not a significant impediment to optical system performance.

Finally, in order to apply the calibration data to real data collected during plasma operation, the *in-situ* calibration data ratio taken from ∼50–320 °C are fit to a function of the same form as the *ex-situ* data, but multiplied by an additional constant to represent the losses in the NSTX IR window to account for the reduced transmission in the MWIR channel relative to the LWIR channel. Demonstration of the suitability of a fit with the same functional form to the *in-situ* data observing the LLD as fit to the *ex-situ* BB data is a strong indication that no significant non-gray body emissivity exists in the observed Li surface. Further confidence is taken from the lack of any significant non-uniformity in the measured *in-situ* integrated emission band ratio versus temperature relationship through the transition from solid to liquid Li around its melting point at 180.54 °C.

V. MEASUREMENTS DURING PLASMA DISCHARGES

Analysis of data captured by the fast IR camera attached to the dual-band adapter during plasma operation in NSTX is carried out by a PYTHON-based automation code for camera control timed to the tokamak discharge clock, and paired with custom-designed software developed image processing and calibration. The latter software is written using the interactive data language in a suite of utilities whose functions include:

- Background subtraction of dark current and bias applied to the imaging detector.
- Isolation of the LWIR and MWIR band image regions on the detector based on pre-selected bounds determined based on the alignment of the dual-band IR adaptor on the IR camera (Figure 7(a)).
- Spatial calibration of the image resulting from taking the LWIR/MWIR ratio of the data with respect to the geometry of the divertor floor in the NSTX device. Spatial alignment is carried out in both $[X,Y]$ and $[r,\theta]$ space (Figure 7(b)). Major features observed under plasma heating include gaps between tiles exposed in the direction of the plasma current, bolt holes in the graphite tiles, the space between the inner and outer divertor (i.e., the "CHI" gap), and edges between the graphite tiles and the LLD plates.

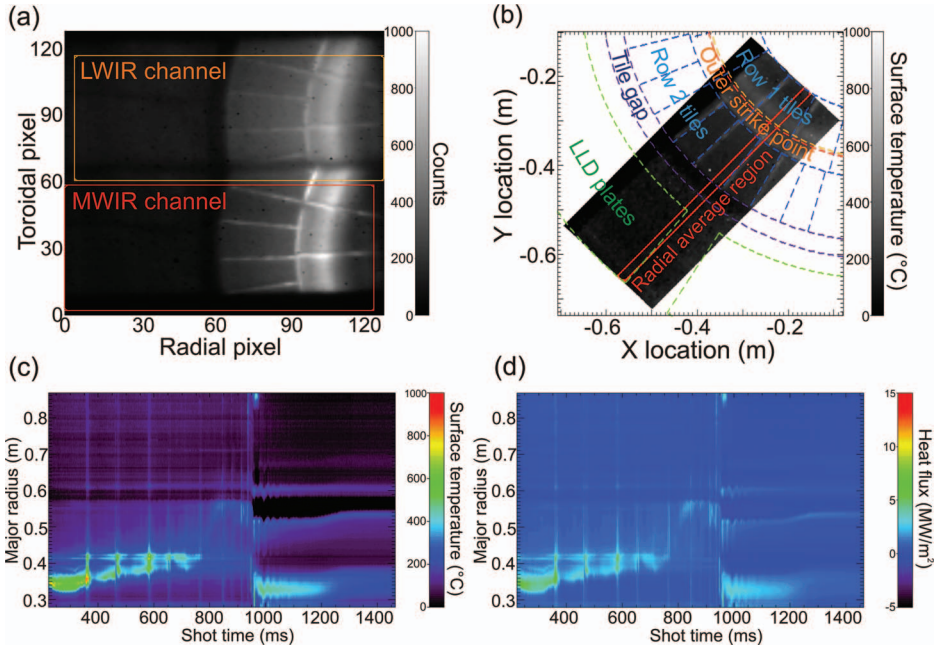

FIG. 7. (a) Sample raw LWIR (top) and MWIR (bottom) data from the dual-band IR adaptor and camera on the NSTX device during a plasma discharge. (b) Spatially calibrated data to both $[X,Y]$ and $[R,\theta]$ coordinate systems showing major features of the NSTX floor. (c) Radially calibrated T_{surf} [°C] profile plotted versus time for the given plasma discharge. (d) Radially calculated heat flux, q [MW/m^2] profile plotted versus time for the same discharge.

- Application of absolute temperature calibrations to both resulting 1D radial profiles, and 2D single-color (i.e., independent MWIR and LWIR) images, and dual-band ratio images (Figure 7(c)).
- Calculation of heat flux impinging on the plasma-facing surfaces using the temporal surface temperature profile applying the 1D Carslaw & Jaeger heat conduction equation[29] and the 2D THEODOR code[30] (Figure 7(d)).

Demonstration of the dual-band IR technique was made in plasma discharges early in the 2010 NSTX operating campaign after a large deposition of Li onto the divertor floor, effectively filling the LLD. Calibrated thermal data from this discharge is shown in Figure 8. Data are averaged over an area defined by ±2 cm in radial extent around the peak of the plasma flux profile (i.e., the "strike point") and a 5 cm extent in the toroidal direction. The fast IR camera was operated at a capture rate of 1.6 kHz beginning 250 ms into the discharge and extending to 1.7 s. Heating of the LLD surface by the plasma takes place from ~300 ms until the end of the discharge at 1.0 s. Temporal gaps in acquired data were found to be due to EM interference caused by the proximity of cabling used by the IR camera to high current-carrying leads (>10 kA) to the toroidal field coils near the camera location; once discovered, these gaps were eliminated.

In processing the data, independent application of each of three separate temperature calibrations are made to the same raw data from the IR camera: the integrated LWIR single-band intensity is calibrated according to surface temperature (red), the integrated MWIR single-band intensity is calibrated according to surface temperature (green), and finally, the integrated LWIR/MWIR dual-band intensity is calibrated according to temperature (blue). Surface temperatures in each case are found to increase upwards of 500 °C for brief periods (~5 ms intervals) then fall to a lower base of ~250 C. Each of the three calibrations result in different surface temperatures, with, in general, the two single-band calibrated results matching better than either one of the single-band results with the dual-band result. After plasma heating ceases and cooling of the near-surface Li by conduction into the bulk of the LLD begins, the calibrated surface temperature is found to reduce monotonically. In the case of the single-band calibrated results, both calibrations suggest that the surface temperature reduces to ~130 C by the final data point. In the case of the dual-band calibrated data, however, the LLD surface temperature is found to approach and level off at a value of ~180 C for at least the period of time in which data is captured. This value is equal to the melting point of Li (180.54 C), and thus suggests that the surface pauses for this time at the temperature of solidification consistent with the release of the latent heat of fusion (i.e., the decrease in enthalpy) which is expected at the phase transition. The observation that the single-band data continues past this point without pause suggested that its result is instead indicative of a change in emissivity associated with the phase transition and not an actual thermal response.

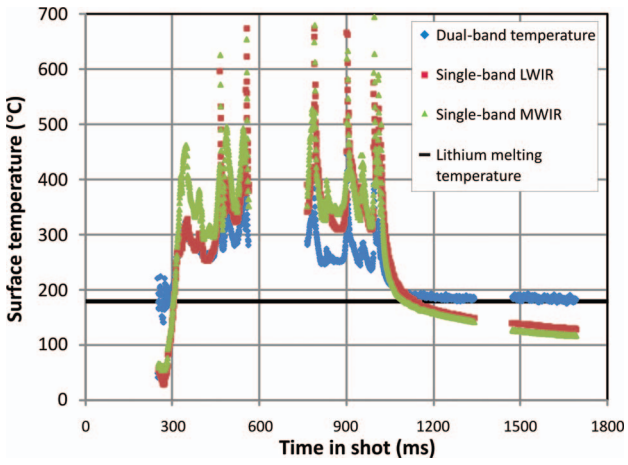

FIG. 8. Peak Li surface temperature on the LLD as calculated by applying each individual integrated band calibration, and the dual-band calibration to the same data collected simultaneously by the IR camera paired with the dual-band IR adapter. After plasma heating is complete, dual-band calibrated data is found to fall to the Li melting temperature as expected, while single-band calibrated data falls monotonically below $T = 180\,^{\circ}\mathrm{C}$.

Finally, it is noted that the surface temperatures derived from each of the single-band calibrations appear to diverge from the temperature calculated based on the dual-band calibration through the period of plasma heating (t = 300–1000 ms) during most of which the surface temperature is measured to be well above the melting temperature of Li. This is hypothesized to be due to accumulation of impurities on the surface (e.g., LiOH, LiC, etc.), and thus indicative of the emissivity of those impurities, and/or due to changing surface characteristics as a consequence of texture of the thin layer where the impurity develops. The effect of this impurity accumulation on the surface layer must be limited, however, due to the resulting post-discharge surface temperature which is dominated by the underlying Li layer.

VI. POSSIBLE SYSTEM UPGRADES

In the current system, a number of improvements are recommended for improved performance. Replacement of the Bay H port ZnSe window with one that is AR-coated for at least 4–10 m would result in a significant gain in overall system transmission, and an associated improvement in SNR. Local LED-based IR source to optimize individual channel projection onto the detector, minimizing the unused portion.

Additionally, a system currently under development also for use on NSTX will incorporate a two-color IR adapter which splits the LWIR band into separate 8–10 μm and 10.5–13.0 μm colors for use with a microbolometer-based IR camera. Due to the relatively low cost of microbolometer cameras and their ability to operate without liquid nitrogen cooling, demonstration of the two-color IR technique in this wavelength range will make it possible to bring the benefits of the integrated intensity ratio approach to a much larger number of IR cameras already operating at fusion facilities around the world.

VII. SUMMARY AND CONCLUSIONS

An innovative optical dual-band infrared imaging adapter has been designed, built, and successfully demonstrated on the NSTX fusion research device. The surface temperature of

lithium as it transitioned from solid to liquid and back was observed both when it was electrically heated without the presence of plasma, and when heated by plasma alone then cooled by conduction. The temperature of Li was measured to have a plateau at its melting point as expected based on the latent heat of fusion. Using a dichoric beamsplitter designed for the MWIR/LWIR bands, the dual-band IR adapter projects the observed image integrated through each band side-by-side on the IR camera detector allowing the ratio of the two bands to be taken and calibrated against surface temperature. In this manner, this adapter allows an existing single-band camera to operate as a dual-band device, thus significantly reducing the effect of the observed material emissivity on the measured surface temperature profile. Compared to dedicated dual-band IR cameras now under development, this technique has the advantage that it allows the single-band camera to operate at its maximum frame rate, and with a significantly reduced cost compared to that of a new dual-band camera. After evaluation using dichroic beamsplitters that separate light in the MWIR or LWIR spectral regions, the two-color imaging adaptor concept may be applied to both existing high- and low-speed IR cameras currently in operation at fusion facilities around the world.

ACKNOWLEDGMENTS

This work was supported by the U.S. Department of Energy (DOE) (Contract Nos. DE-AC05-00OR22725 and DE-AC02-09CH11466). The authors would also like to thank Jeremy Graham and Martyn Reynolds of CAIRN Research, and Gary Herrit of II-VI Infrared for their advice and design expertise. Finally, the authors would like to extend individual thanks to Scott Gifford, Tom Holoman, Ron Jakober, and the rest of the Princeton Plasma Physics Laboratory team for their technical assistance and effort.

[1]J.-W. Ahn, R. Maingi, D. Mastrovito, and A. L. Roquemore, Rev. Sci. Instrum. **81**, 023501 (2010).
[2]R. E. Nygren, H. C. Harjes, P. Wakeland, R. Ellis, H. W. Kugel, R. Kaita, L. Berzak, L. Zakharov, and B. Ehrhart, Fusion Eng. Des. **84**, 1438 (2009).
[3]H. W. Kugel, M. G. Bell, L. Berzak, A. Brooks, R. Ellis, S. Gerhardt, H. Harjes, R. Kaita, J. Kallman, R. Maingi, R. Majeski, D. Mansfield, J. Menard, R. E. Nygren, V. Soukhanovskii, D. Stotler, P. Wakefield, and L. E. Zakharov, Fusion Eng. Des. **84**, 1125 (2009).
[4]E. M. Hollmann, A. Yu. Pigarov, and R. P. Doerner, Rev. Sci. Instrum. **74**, 3984 (2003).
[5]R. W. Moir, LLNL Report No. UCRL-ID-134612, 1999.
[6]E. Hagen and H. Rubens, "Über Beziehungen des Reflexions- und Emissionsvermögens der Metalle zu ihrem elektrischen Leitvermögen," Ann. Phys **316**, 873 (1903).
[7]M. Bramson, *Infrared Radiation* (Plenum, New York, 1968), p. 127.
[8]K. Chrzanowski, Infrared Phys. Technol. **36**, 679 (1995).
[9]L. Ibos, M. Marchetti, A. Boudenne, S. Datcu, Y. Candau, and J. Livet, Meas. Sci. Technol. **17**, 2950 (2006).
[10]A. Seifter, in Proceedings of the XVII IMEKO World Congress, TC12, Crotia, 22–27 June 2003.
[11]R. Maingi, M. G. Bell, R. E. Bell, J. Bialek, C. Bourdelle, C. E. Bush, D. S. Darrow, E. D. Fredrickson, D. A. Gates, M. Gilmore, T. Gray, T. R. Jarboe, D. W. Johnson, R. Kaita, S. M Kaye, S. Kubota, H. W. Kugel, B. P. LeBlanc, R. J. Maqueda, D. Mastrovito, S. S. Medley, J. E. Menard, D. Mueller, B. A. Nelson, M. Ono, F. Paoletti, H. K. Park, S. F. Paul, T. Peebles, Y.-K. M. Peng, C. K. Phillips, R. Raman, A. L. Rosenberg, A. L. Roquemore, P. M. Ryan, S. A. Sabbaugh, C. H. Skinner, V. A. Soukhanovskii, D. Stutman, D. W. Swain, E. J. Synakowski, G. Taylor, J. Wilgen, J. R. Wilson, G. A. Wurden, S. J. Zweben, and the NSTX Team, Plasma Phys. Controlled Fusion **45**, 657 (2003).
[12]R. Reichle, J.-P. Lasserre, F. Oelhoffen, C. Desgranges, F. Faisse, L. Eupherte, C. Pocheau, and M. Todeschini, Phys. Scr. **T138**, 014029 (2009).
[13]M.-H. Aumeunier and J.-M. Travere, Rev. Sci. Instrum. **81**, 10E524 (2010).
[14]V. A. Soukhanovski, Rev. Sci. Instrum. **79**, 10F539 (2008).
[15]See www.cfa.harvard.edu/HITRAN for HITRAN database, and described in L. S. Rothman, I. E. Gordon, A. Barbe, D. Chris Benner, P. F. Bernath, M. Birk, V. Boudon, L. R. Brown, A. Campargue, J.-P. Champion, K. Chance, L. H. Coudert, V. Dana, V. M. Devi, S. Fally, J.-M. Flaud, R. R. Gamache, A. Goldman, D. Jacquemart, I. Kleiner, N. Lacome, W. G. Lafferty, J.-Y. Mandin, S. T. Massie, S. M. Mikhailenko, C. E. Miller, N. Moazzen-Ahmadi, O. V. Naumenko, A. V. Nikitin, J. Orphal, V. I. Perevalov, A. Perrin, A. Predoi-Cross, C. P. Rinsland, M. Rotger, M. Šimečková, M. A. H. Smith, K. Sung, S. A. Tashkun, J. Tennyson, R. A. Toth, A. C. Vandaele, and J. Vander Auwera, J. Quant. Spectrosc. Radiat. Transf. **110**, 533 (2009).
[16]H. Madura, M. Kastek, and T. Piatkowski, Infrared Phys. Technol. **51**, 1 (2007).
[17]H. W. Kugel, D. Mansfield, A. L. Roquemore, J. Timberlake, H. Schneider, M. G. Bell, M. Jaworski, R. Kaita, J. Kallman, T. Abrams, B. LeBlanc, C. H. Skinner, L. Zakharov, S. Zweben, R. Maingi, A. G. McLean, J. W. Ahn, R. E. Nygren, V. A. Soukhanovskii, J. P. Allian, B. Heim, and C. N. Taylor, IAEA2010, FTP/3-6Ra (IAEA, 2010). Also found online at www-pub.iaea.org/mtcd/meetings/PDFplus/2010/cn180/cn180_papers/ftp_3-6ra.pdf.
[18]C.-D. Wen and I. Mudawar, Int. J. Heat Mass Transfer **49**, 4279 (2006).
[19]M. Rosenberg, R. D. Smirnov, and A. Yu. Pigarov, Fusion Eng. Des. **84**, 38 (2009).
[20]T. J. Tanaka, T. J. Lutz, J. M. McDonald, R. E. Nygren, K. P. Troncosa, R. Bastasz, and M. Clift, APEX meeting presentation, UCLA, April 24–May 2, 2001. Also found online at www.fusion.ucla.edu/apex/meeting15/Apex4_01-tanaka.pdf.
[21]See www.sbfp.com for Santa Barbara Focal Plane, Goleta, California, USA.
[22]See www.lambda.cc for Lambda Research Optics, Costa Mesa, California, USA.
[23]See www.cairnweb.com for CAIRN Research Limited, Faversham, Kent, UK.
[24]See www.iiviinfrared.com for II-VI Infrared, Saxonburg, Pennsylvania, USA.
[25]Y. Tamagawa, Opt. Rev. **4**, 321 (1997).
[26]J.-I. Kudo, H. Wada, T. Okamura, M. Kobayashi, and K. Tanikawa, Opt. Eng. **41**, 1787 (2002).
[27]C. Londoño and P. P. Clark, Appl. Opt. **31**, 2248 (1992).
[28]See www.reynardcorp.com for Reynard Corporation, San Clemente, California, USA.
[29]H. S. Carslaw and J. C. Jaeger, *Conduction of Heat in Solids* (Oxford University Press, New York, 1959).
[30]A. Herrmann, W. Junker, K. Gunther, S. Bosch, M. Kaufmann, J. Neuhauser, G. Pautasso, Th. Richter, and R. Schneider, Plasma Phys. Controlled Fusion **37**, 17 (1995).